

Dust-to-gas ratios in the Kepler supernova remnant

M. Contini^{1,2}

¹ Instituto de Astronomia, Geofísica e Ciências Atmosféricas - USP, Brazil

² School of Physics and Astronomy, Tel Aviv University, Tel Aviv 69978, Israel

Received ;

Abstract.

A new method to evaluate the dust-to-gas ratios in the Kepler SNR is presented. Dust emission in the infrared and bremsstrahlung are calculated consistently, considering that dust grains are collisionally heated by the gas throughout the front and downstream of both the expanding and the reverse shocks. The calculated continuum SED is constrained by the observational data. The dust-to-gas ratios are determined by the ratio of the dust emission bump and bremsstrahlung in the infrared. The shell-like morphological similarity of X-ray and radio emission, and of the H α and infrared images confirms that both radio and X-ray emissions are created at the front of the expanding shock and that dust and gas are coupled crossing the expanding and reverse shock fronts. The results show that large grains with radius of $\sim 1 \mu\text{m}$ with dust-to-gas ratios $< 4 \cdot 10^{-3}$ survive sputtering and are heated to a maximum temperature of 125 K downstream of the shock expanding outwards with velocity of about 1000 km s $^{-1}$. The high velocity shocks become radiative for dust-to-gas ratios $> 10^{-3}$. Such shocks do not appear in the NE region, indicating that dust grains are not homogeneously distributed throughout the remnant. Smaller grains with radius of about $0.2\mu\text{m}$ and dust-to-gas ratios of $\sim 4 \cdot 10^{-4}$ are heated to a maximum temperature of ~ 50 K downstream of the reverse shock corresponding to velocities of about 50 km s $^{-1}$. A maximum dust mass $< 0.16 \text{ M}_\odot$ is calculated.

Key words. ISM:supernova remnants-individual objects:Kepler

1. Introduction

Since the first identification by Baade (1943) the remnant of the Kepler supernova (SN) which exploded in 1604, has been observed in the different wavelength ranges.

van den Bergh & Kemper (1977) studied brightness variations and proper motions of the filaments in the supernova remnant (SNR). Spectrophotometry data of the bright-western knots in the spectral range 3700-10,500 Å were presented by Dennefeld (1982). Observations in the optical range for single bright knots were obtained by Leibowitz & Danziger (1983) and by Blair, Long & Vancura (1991).

Data in the X-ray (e.g. Hughes 1999) and in the radio (e.g. DeLaney et al. 2002) ranges were also recently presented. Morgan et al (2003) provided SCUBA data of the continuum in the far infrared (450 and 850 μm), so the information about the infrared (IR) emission is rather complete.

The main results obtained from the interpretation of the line spectra (Blair et al) are, in particular, that the emitting gas has high densities ($\geq 1000 \text{ cm}^{-3}$), that the N/H relative abundance is ~ 3.5 times higher than solar, and H α line profiles display both broad and narrow components. A distance of 5 kpc was consistently determined.

Send offprint requests to: M. Contini

The origin of Kepler SNR emitting features is explained by the interaction of the high velocity ejecta with the ambient medium (Decourchelle & Pretre 1999) and is very similar to that found for other SNRs, e.g. Cassiopeia A (Chevalier & Oishi 2003), namely, "that the observed shock wave positions and expansions can be interpreted in a model of supernova interaction with a freely expanding stellar wind." The collision with ambient matter leads to the formation of two shock fronts: a shock propagating outwards throughout the circumstellar/interstellar medium and one propagating in reverse throughout the ejecta in the direction opposite to the propagation of the blast wave. The gas in the knotty regions of Kepler SNR is ionized and heated to relatively high temperatures ($\leq 3 \cdot 10^7$ K) downstream of the shock which expands with velocities of 1000 -1500 km s $^{-1}$. The reverse shock, on the other hand, propagating with velocities of ~ 50 km s $^{-1}$ in the opposite direction, leads to lower gas temperatures. The velocities are reduced by the density gradient of the ejected matter. The circumstellar origin of the optical emitting gas suggested that Kepler's SN was actually of Type Ib (Bandiera 1987).

Very recently Morgan et al (2003) addressed the problem of dust in Kepler SNR in terms of its total mass and its origin from a massive star. They claim that dust formation in SNe is an important process, but dust in SNRs has been detected in small quantities.

In this work we will use the method adopted by e.g. Contini & Contini (2003) to calculate the dust-to-gas ratios in the starburst regions of luminous infrared galaxies and by Contini, Viegas & Prieto (2004) for Seyfert galaxies. Namely, dust-to-gas ratios are calculated by modeling the spectral energy distribution (SED) of the continuum in the optical-IR frequency range.

At the shock front edge of the emitting nebulae, the gas is collisionally heated to relatively high temperatures which depend on the shock velocity. Dust and gas are coupled crossing the shock front, mutually heating and cooling by collisions (Dwek & Arendt 1992, Viegas & Contini 1994, Contini et al. 2004). The temperature of the grains depends on the temperature of the gas and, therefore, the maximum temperature of dust depends on the shock velocity (Contini et al. 2004). The observational data constrain the model which better explains both the bremsstrahlung and reradiation by dust. Particularly, the ratio between the dust radiation flux in the IR and bremsstrahlung depends on the dust-to-gas ratio.

However, the modeling of the continuum SED must be cross-checked by the modeling of the line spectra, which is strongly constraining.

In this paper I would like to find out the physical conditions in the different regions of Kepler SNR, as well as the dust-to-gas ratios, by consistent model calculations, which take into account the results of previous investigations.

The SUMA code (Viegas & Contini 1994, Contini & Viegas 2001 and references therein), which is adapted to the calculation of gas and dust spectra emitted downstream of a shock front, is adopted.

The general models are presented in Sect. 2. The models specifically calculated for the Kepler SNR appear in Sect. 3.1. The comparison of the spectra with the data is discussed in Sect. 3.2 and cross checked by the fit of the continuum SED in Sect. 3.3. Discussion and concluding remarks follow in Sect. 4.

2. The models

The models result from numerical simulations with the code SUMA that requires the following input parameters: the shock velocity, V_s , the pre-shock density, n_0 , the pre-shock magnetic field, B_0 , the chemical composition of the gas, and a dust-to-gas ratio d/g by number. The initial radius of the grains a_{gr} is also required. The geometrical thickness of the cloud, D , is an input parameter in the case of matter-bound models. A plan-parallel symmetry is adopted with the calculations starting at the shocked edge. To perform the calculations a cloud is divided into a number of slabs (up to 300) within which the physical conditions are considered homogeneous. The geometrical thickness of the slabs is automatically calculated by SUMA according to the gradient of the temperature downstream, in order to calculate as smoothly as possible the distribution of the physical conditions throughout the cloud. The first slabs in the immediate post shock region show the maximum temperature which depends on V_s . These slabs can be relatively large because recombination coefficients are lower the higher the temperature. The geometrical thickness of the slab closest to the shock front is therefore determined by the model.

2.1. Calculation of the spectra

The spectra emitted from gas downstream of the shock front, are calculated with a large number of equations, starting with those (e.g. Cox 1972) for the conservation of mass, momentum, and energy, which lead to the compression equation. Once the physical conditions are determined in a given slab, the ionization equations for all the elements are resolved. Then, the cooling rate is calculated from the energy losses by free-free, free-bound, and line emission, as well as by collisional heating of dust grains (Dwek & Arendt 1992).

The distributions of the electron temperature and of the electron density downstream are thus obtained, as well as the stratification of the different ions for the different elements.

The structure of the gas downstream is determined by the shock. Near the shock front edge, the gas is collisionally heated to relatively high temperatures ($T \propto V_s^2$) which determine the maximum of bremsstrahlung at higher frequencies. Notice that both free-free and free-bound processes are included in the calculation of the continuum.

Due to dust collisional heating by gas, the maximum temperature of dust depends on the shock velocity, which therefore determines the frequency of the reradiation peak in the infrared. An analytical relation between the wavelength of the maximum intensity of dust reradiation in the IR spectrum and shock velocity is given by Draine (1981).

The grains are also heated by radiation. However, the only radiation source in SNR is diffuse secondary radiation from the hot slabs of gas, collisionally heated by the shock. Diffuse radiation ionization rates prevail on collision rates only when the gas temperature has dropped to $T \leq 10^4$ K. Radiation heating of grains, which is consistently calculated by SUMA, leads to low temperatures of the grains, < 16 K in high velocity clouds and < 30 K in low velocity clouds.

In models accounting for the shock, sputtering changes the initial grain-size distribution, creating a deficiency of small grains compared to their pre-shock abundances (Dwek, Foster, & Vankura 1996). The grain size distribution depends on the shock velocity and on the density of the medium. The sputtering rate increases when the dust is in motion. The present calculations account for the sputtering in the different zones downstream of the shock front, so, the distribution of the grain sizes along the cloud is automatically derived by SUMA starting from an initial size.

Generally, three populations of grains are adopted to fit the average interstellar extinction curve: large grains of silicate with radius $a_{gr} \sim 0.01$ - 1.0 μm , small graphite particles ($a_{gr} < 0.05$ μm), and polycyclic aromatic hydrocarbons (PAH) which correspond to single molecules of 25 carbon atoms and clusters of 10-20 molecules. Small graphite particles and PAH are underabundant with respect to the interstellar medium by factors of 10 or more (Siebenmorgen et al 1999). Moreover, they are rapidly destroyed by sputtering across the shock front (Contini & Contini 2003, Contini et al. 2004). So, only silicate grains are considered.

Depending on the temperature distribution in the cloud, bremsstrahlung may contribute to the infrared continuum (see, for instance, Contini & Viegas-Aldrovandi 1990, fig 2c). The

Table 1. The models selected from the grid

model	m1	m2	m3	m4	m5	m6	m7	m8	m9	m10
V_s (km s $^{-1}$)	50	50	50	60	300	400	700	800	1000	1000
n_0 (cm $^{-3}$)	3(3)	6(3)	9(3)	9(3)	300	300	60	40	10	100
d/g(10 $^{-14}$)	1	1	1	1	1	1	4	5	9	0.5
[OII]3727+3729	22.0	13.0	8.6	8.0	5.0	3.50	7.6	12.7	11.2	4.7
[NeIII]3869+3968	.015	.010	.007	.33	1.58	1.890	2.1	2.19	2.65	1.08
[SII]4069+4076	1.80	1.90	2.10	1.70	.90	1.400	7.0	0.8	1.5	1.5
[OIII]4363	.006	.004	.002	.20	1.00	1.110	1.04	1.11	0.27	0.17
HeII 4684	.00	.00	.00	.00	.08	.140	0.27	0.24	0.16	0.3
[OIII]4959+5007	.12	.07	.05	2.89	12.30	12.800	13.1	13.7	3.53	2.17
[FeII]5159	.25	.20	.19	.20	.23	.450	0.2	0.25	2.2	0.7
[NI]5200	.02	.01	.007	.005	.06	.140	0.09	0.13	2.7	0.14
[FeIII]5270	.34	.35	.34	.28	.30	.110	0.089	0.11	0.035	0.015
[NII]5755	.54	.62	.63	.63	.24	.260	0.177	0.22	0.1	0.07
He I 5876	.11	.14	.116	.18	.33	.330	0.21	0.23	0.6	0.2
[OI]6300+6364	.64	.48	.46	.50	1.10	2.450	0.88	1.1	14.	3.45
[NII]6548+6583	8.00	7.40	6.27	5.12	2.90	2.860	3.25	4.14	6.26	3.5
[SII]6717	.43	.24	.18	.10	.37	.630	0.6	0.93	16.7	0.7
[SII]6730	.90	.55	.41	.24	.78	1.330	1.16	1.7	14.2	1.5
[OII]732+7330	10.00	12.30	12.00	13.00	5.50	5.700	3.88	4.6	0.89	0.8
[SIII]9069+9532	1.90	2.00	1.54	2.16	1.14	1.120	1.0	1.17	0.29	0.13
[CI]9823+9849	.30	.17	.15	.50	1.580	.160	0.39	1.3	8.8	0.52
$H\beta_{abs}^1$	1.	2.	3.7	4.	1.4	1.7	0.53	0.33	0.38	9.13

¹ 10 $^{-3}$ erg cm $^{-2}$ s $^{-1}$

intensity of dust IR emission relative to bremsstrahlung depends on the dust-to-gas ratio. Usually the dust contribution dominates in the far infrared range but in the near-IR, both processes may contribute to the continuum (see Sect. 3.3).

Finally, very seldom the line and continuum spectra of the galaxies can be reproduced by single-cloud models; on the other hand, multi-cloud models are generally required to explain the multiwavelength spectrum and are obtained as a weighted average of the single-cloud models. Multi-cloud models lead to IR bumps wider than black body curves.

The modeling of a spectrum consisting of only a few lines, deserves a further comment. In fact, it is reasonable only when such a spectrum belongs to a series of spectra observed in neighbour regions, for a certain object. In this case, the input parameters which are not likely to change in neighbour regions, e.g. relative abundances and the pre-shock magnetic field, are determined from the spectra rich in number of lines, while, the shock velocity is roughly deduced from the line FWHM. If the observations do not provide the lines whose ratio depends on the density of the emitting gas, the pre-shock density can be roughly obtained from the modeling of neighbour regions. On the other hand, the geometrical thickness of the cloud is a free parameter because it depends on fragmentation. Some times, different combinations of the input parameters lead to very similar results for one or two of the most significant line ratios. So, the final choice of the model is determined by consistency on a large scale. Nevertheless, spectra showing only a few lines should be ignored, if they are not indispensable.

2.2. Choice of the input parameters

A first choice of V_s comes from the FWHM of the observed line profiles and, generally, from the intensity ratio of lines from different ionization levels. The range of n_0 is suggested by the [SII] 6717/6730 line ratios. Notice, however, that the density of the line emitting gas downstream is higher than n_0 by a factor ≥ 10 due to compression.

In matter-bound models the geometrical thickness of the nebula is roughly determined by the intensity of low-level and neutral lines.

The magnetic field and the density are linked through the compression equation (Cox, 1972) which is calculated in each slab of the gas downstream, leading to the density profile. The range of B_0 is suggested by the results obtained for the other supernova remnants (Cygnus Loop, Cassiopeia A, etc) and for the interstellar medium, $B_0=10^{-6} - 10^{-5}$ gauss (Contini et al. 1980, Contini & Shaviv 1982, Contini 1987). The choice of the pre-shock magnetic field in modeling is also constrained by the best agreement of all the calculated line ratios with the observational data.

The models discussed here have been obtained assuming as a first choice cosmic chemical abundances for He, C, N, O, Ne, Mg, Si, S, Ar, and Fe (Allen 1973). The elements which reveal depletion from the gaseous phase by trapping into grains are carbon, silicon, magnesium, iron, etc. Most of their lines are prominent in the UV and in the infrared spectra, while the observed lines are actually in the optical- near infrared. Moreover, sulphur can be trapped into CS diatomic molecules.

The dust-to-gas ratios are constrained by the SED of the continuum in the IR range. It is found that only large grains

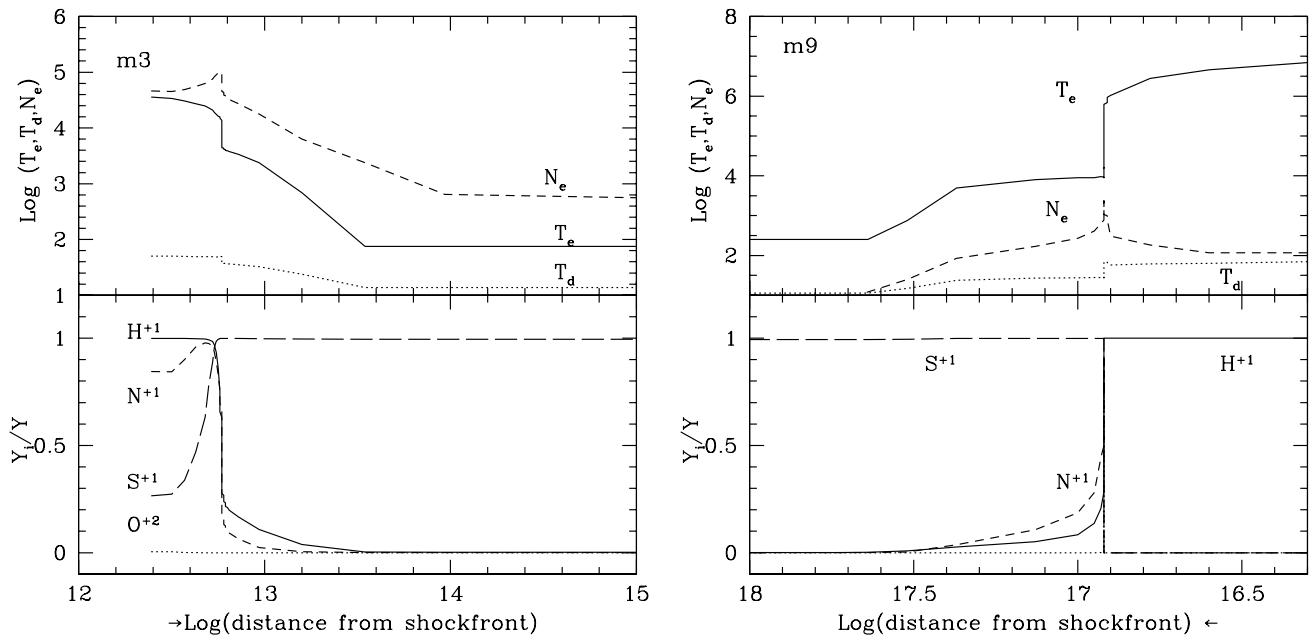


Fig. 1. The distribution of the electron temperature (solid line), of the dust temperature (dotted line), and of the electron density (dashed line) downstream (top panels) and of the fractional abundances of some significant ions downstream (bottom panels) for model m3 (left diagram) and model m9 (right diagram). H^{+1}/H : solid line; N^{+1}/N : short-dashed line; S^{+1}/S : long-dashed line; O^{+2}/O : dotted line

($a_{gr} \sim 1 \mu\text{m}$) survive sputtering in high velocity shocks. The sizes of grains adopted for low velocity shocks are constrained by the data at long wavelengths (Contini et al. 2004, fig. 7, left panel) and $a_{gr} = 0.2 \mu\text{m}$ is obtained by comparison with SCUBA data. The contributions of dust emission from all the slabs downstream are summed up and lead to the IR bump.

3. Modeling Kepler SNR spectra

The FWHM of the observed $H\alpha$ line profile suggests that two kinds of shocked clouds contribute to the spectra from each observed region, those with high ($V_s \sim 1000 \text{ km s}^{-1}$) and those with low velocities ($V_s \sim 50 \text{ km s}^{-1}$). The pre-shock densities are high enough as to obtain $[\text{SII}]6713/[\text{SII}] 6730 < 1$. Considering the adiabatic jump at the shock front and that compression downstream increases with the shock velocity, low velocity clouds must be characterized by high pre-shock densities, while high velocity clouds which propagate outwards and have reached the outskirts of the SNR have lower densities. This will lead to non radiative shocks characterized by very long recombination times of the gas downstream. Recombination coefficients decrease at high temperatures and if the densities are too low to speed up the cooling process, the temperatures within the cloud will never drop below $T = 10^5 \text{ K}$, which are critical to the optical (and UV) line emission. In other words, these models are matter-bound. On the other hand, X-rays which correspond to bremsstrahlung from high temperature gas are actually observed, revealing the presence of these clouds.

Adopting dust-to-gas ratios as those predicted for Kepler's SNR by other authors (e.g. Morgan 2003) and confirmed cross-

checking the results of the present paper (Sect. 4), the energy losses by collisional heating of grains prevail downstream of high velocity clouds, even characterized by a low density, leading to cooling times much shorter than the age of the remnant (400 yr). This is an important issue in view of the choice of the models. In particular, d/g should be higher by at least a factor of 3 than normal values (10^{-14} by number) and the grain radius large enough ($a_{gr} \sim 1 \mu\text{m}$) to survive sputtering.

Due to fragmentation which follows from turbulence in shock dominated regimes, many different emitting nebulae (clouds) coexist in each region, so, to model the corresponding observed spectrum, different single-cloud models must be summed up adopting relative weights in order to obtain the best agreement with the data. Notice that the structure of the observed regions is very complex, and a perfect fit to the observed spectra by some typical models is senseless. So, in the following we will try to explain only the most significant line ratios for each of the observed spectra.

3.1. The grid

In Table 1 we present the single-cloud models selected from a large grid covering all the possible physical conditions which are consistent with the Kepler SNR events. Each of the models leads to the rough fit of some of the observed line ratios. We reduced the number of models to a minimum of prototypes, because modeling provides only an approximated picture. The ranges of the input parameters were chosen by the observational evidence and by a first modeling of some significant line ratios ($[\text{OIII}] 4959+5007$, $[\text{OII}] 3727+3729$, $[\text{OI}] 6300+6364$, $[\text{NII}] 6548+6583$, and $[\text{SII}] 6717$ and 6730), con-

Table 2. Comparison of calculated with observed line ratios ($H\beta=1$) from the whole remnant

line	obs. ¹	obs. ²	M1	M2
[OII] 3727+3729	6.74	(>7)	6.7	8.6
[NeIII] 3869+3968	-	0.21	0.58	0.58
[SII] 4069+4076	2.87	1.37	1.6	1.8
[OIII] 4363	0.37	0.14	.27	.33
HeII 4686	-	0.01	0.06	0.04
[OIII] 4959+5007	4.3	3.3	3.6	4.0
[FeII] 5159	-	0.17	0.3	0.26
[NI] 5199+5200	-	0.04	0.1	0.07
[FeIII] 5270	-	0.04	0.2	0.29
[NII] 5755	0.26	0.11	0.4	0.5
HeI 5876	0.15	0.12	0.18	0.19
[OI] 6300+6364	1.75	1.52	1.2	1.05
[NII] 6583+6548	7.16	7.0	4.8	5.4
[SII] 6717	0.5	0.55	0.6	0.5
[SII] 6730	1.12	1.12	1.1	0.83
[SIII] 9069+9532	0.48	-	1.3	1.4
[CI] 9823+9849	0.20	-	0.3	0.46
w(m1)	-	-	0	3
w(m3)	-	-	1.3	5
w(m4)	-	-	1	0
w(m5)	-	-	0	3
w(m6)	-	-	1	3
w(m7)	-	-	0	1
w(m8)	-	-	1.3	0
w(m9)	-	-	0	1

¹ Dennefeld (1982); merged 1979 spectrum corrected for reddening by $c=1.69$

² Leibowitz & Danziger (1983): dereddened by $c=1.46$

sidering that, finally, only multi-cloud models will be compared with the data.

The first three rows of Table 1 show the model input parameters. Then, the calculated line ratios to $H\beta=1$ are given, followed by the $H\beta$ absolute flux in the last row. $B_0=10^{-5}$ gauss is adopted for all the models. The models in Table 1 are ordered by increasing shock velocities.

The selected models (Table 1) show three different types characterized by 1) low velocity shocks with $V_s \sim 50 \text{ km s}^{-1}$ and $n_0 \geq 3000 \text{ cm}^{-3}$ (m1-m4), 2) intermediate shocks ($V_s=300,400 \text{ km s}^{-1}$) which propagate outwards and were decelerated by impinging on high density debris of previously ejected matter (m5 and m6), and 3) high velocity shocks with $V_s \geq 700 \text{ km s}^{-1}$, $n_0 < 100 \text{ cm}^{-3}$, and $d/g > 3 \cdot 10^{-14}$ (m7-m9).

The observed FWHMs suggest that shocks with $V_s \sim 50 \text{ km s}^{-1}$ must be accounted for (m1, m2, m3, m4). The corresponding pre-shock densities are $> 1000 \text{ cm}^{-3}$ in order to obtain $[\text{SII}] 6717/6730 < 1$ downstream. The spectra show rather high $[\text{OII}]/H\beta$ and very low $[\text{OIII}]/H\beta$. Interestingly, the $[\text{NII}] 6583+6548/H\beta$ line ratios are similar to the observed ones, without adopting N/H higher than cosmic, while, $[\text{SII}] 6717/H\beta$ and $[\text{SII}] 6730/H\beta$ are very low. Notice that high $[\text{NII}]/[\text{SII}]$ line ratios are characteristic of the observed spectra (Tables 2-6). Actually, the first ionization potential of nitrogen is higher than that of hydrogen, while the first ionization poten-

tial of sulphur is lower. So, the $[\text{NII}]$ and $[\text{SII}]$ lines are emitted from gas in different physical conditions, which rapidly change downstream within small distances (see Fig. 1, left diagram).

The observed large FWHMs lead to models with $V_s \geq 700 \text{ km s}^{-1}$ and relative low $n_0 = 30-60 \text{ cm}^{-3}$ (m7, m8). These models show $[\text{OIII}]/H\beta$, $[\text{OII}] 3727+3729/H\beta$, $[\text{NII}]/H\beta$, and $[\text{SII}]/H\beta$ higher than those calculated by models with $V_s = 300 - 400 \text{ km s}^{-1}$ and $n_0 = 300 \text{ cm}^{-3}$ (m5, m6), but show lower $[\text{OII}] 7320+7330/H\beta$.

Model m9 shows peculiar line ratios, because a high V_s leads to a strong compression of the intermediate-level line (e.g. $[\text{OIII}]$) emitting region, and to a large zone of gas with $T_e < 10^4 \text{ K}$ (Fig. 1, right) which corresponds to strong low level lines ($[\text{OI}]$, $[\text{OII}]$, $[\text{NII}]$, $[\text{SII}]$, etc). Model m10 was added in Table 1 after discussing the SED of the continuum (Sect. 3.3).

The distribution of the electron temperature, of the electron density, and of the fractional abundance of the most significant ions as function of distance from the shock front (in cm) are presented in Fig. 1, for models m3 and m9. Model m3 (left diagram) represents the nebula downstream of the reverse shock which is characterized by low V_s and high n_0 , while model m9 (right diagram) represents the nebula downstream of the shock propagating outwards. Therefore, the shock front is shown on opposite edges in the two diagrams.

The emitting clouds are radiation bound. The ionized region is rather narrow ($\sim 10^{13} \text{ cm}$) in the low velocity model m3 (Fig. 1, left panel). On the other hand, model m9 shows a high temperature zone of $\sim 10^{17} \text{ cm}$ (Fig. 1, right panel) which is reasonable compared to the SNR diameter (3.8 pc), calculated adopting a Kepler SNR distance to Earth of 5 kpc (Blair et al.). The high dust-to-gas ratio ($9 \cdot 10^{-14}$) corresponding to model m9 leads to a cooling time $< 60 \text{ yr}$ in the downstream region.

3.2. Line spectra

The data used for modeling the line spectra come from the following observations. Spectrophotometry data of the bright-western knots covering the spectral range 3700-10,500 Å were obtained during 1979-1980 with the Boller and Chivens spectrograph attached to the ESO 3.6 telescope and were presented by Dennefeld (1982). Observations in the optical range for single bright knots in different positions and the integrated spectrum obtained in the Anglo-Australian 3.9m Telescope come from Leibowitz & Danziger (1983). Blair et al. (1991) presented optical CCD/interference filter imagery and long-slit CCD spectrophotometry of the Kepler SN remnant obtained by the 2.5m DuPont telescope at Las Campanas Observatory. Although Blair et al. data cover a relatively reduced wavelength range, the single spectra observed in more than 20 regions, provide the tools for modeling the SNR extended area.

The mean reddening $E(B-V)$ to Kepler's SNR is 0.9 ± 0.1 (Blair et al.), lower than $E(B-V)=1.1$ given by Leibowitz & Danziger.

The comparison between calculated and observed (reddening corrected) line ratios to $H\beta=1$ is presented in Tables 2-6. The spectra were observed by Dennefeld (1982), Leibowitz & Danziger (1983), and Blair et al. (1991). When the $H\beta$ line is

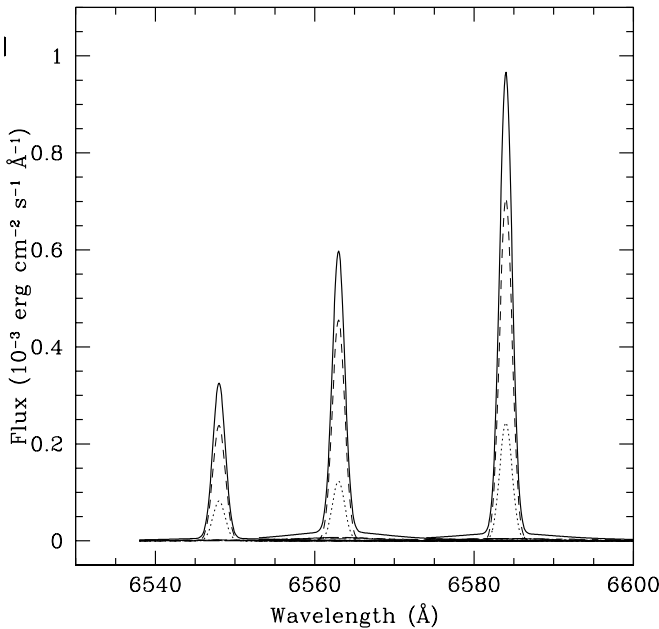


Fig. 2. [NII] 6548, [NII] 6583, and H α line profiles (solid lines) calculated by model MB3 for region D3 observed by Blair et al (1991). Dotted line correspond to model m1, short-dashed line to m3. The fluxes are calculated at the emitting nebula.

not observed we adopt H α /H β =3. The weights of the corresponding single-cloud models and the conversion factors (see Sect. 3.3) appear in the bottom of the tables.

We will aim at fits such that the discrepancies between the calculated line ratios and the observed ones are less than a factor of 2, which accounts for observational errors and modeling approximation (atomic coefficients, etc.). However, not always the agreement is satisfying for all the lines. To have a better fit we should consider a larger number of single-cloud models (see, for instance, region D55 in Table 5). Recall that we are interested mainly in the calculation of the dust-to-gas ratios, therefore, in some regions which are less constrained by spectra poor in number of lines, the fit is not sufficient, leading to discrepancies beyond a factor of 2.

The two observed spectra shown in Table 2 which correspond to integrated data by Dennefeld (1982) and Leibowitz & Danziger (1983) are similar enough. The two multi-cloud models which better explain them correspond to different weights of the single-cloud models. In Table 3 the models are compared with observations in the different regions in the western side of the remnant by Leibowitz & Danziger (1983, Plate 3).

The spectra observed by Blair et al. in the different regions are generally satisfactorily explained by modeling (Tables 4-6). In the top of the tables the observed emission regions and their rough location (D'Odorico et al. 1986) in the SNR are indicated.

The data corresponding to regions D41,45 (Blair et al.) are not considered, because the spectrum is very poor in number of lines. Actually, it is the only position showing very low densities ([SII] 6717/6730 > 1) in the emitting gas. Blair et al claim

that "this emission is not simply a superposition of a non radiative and typical (for Kepler SNR) radiative filament."

The detection of [NII] 6583+ with a FWHM of ~ 40 km s $^{-1}$ (Sollerman et al, Table 1) from a Balmer dominated region (e.g. D49, D50) is explained by the reverse shock, which should be summed up adopting a very small weight compared with that of the high velocity model (> 1000 km s $^{-1}$). Sollerman et al claim that the [NII] emission from D49 and D50 cannot be produced in a cooling zone in Balmer - dominated knots. So, the remaining possibility is ahead of the Balmer-dominated shock, due to Alfvén wave activity in a cosmic ray precursor. Table 1 shows that models calculated with low V_s show very high [NII]/H β line ratios relative to [SII]/H β , therefore, the only narrow lines observable are those of [NII], and perhaps [OII], which unfortunately, were not included in the spectra. Blair et al notice that D47 and D48 with peak at 6584 ([NII]), represent a transition filament implying a minimum shock velocity of 815 km s $^{-1}$.

Two spectra, D56 and P2D1 (P2,diff1) in Table 5, are explained by single-cloud models, m5 and m6, respectively. However, the modeling is less constrained by the small number of observed lines.

Summarizing, the present modeling confirms that N/H relative abundance higher than solar should be adopted, in agreement with previous modeling, however, by a factor <2, which is lower than the factor of ~ 3.5 , suggested by Blair et al. This leads to N/H < 1.8 10 $^{-4}$. Notice that models in group 1), corresponding to the slow shock, and model m9 show rather high [NII] 6583+/H β ratios (> 5). So, in the multi-cloud models which better fit the spectra, the ratios of calculated to observed [NII]/H β are closer to 1, the higher the relative weight of these models. On the contrary, Fe lines are overpredicted by the models, indicating that Fe could be depleted from the gaseous phase.

Tables 2 and 3 show that models with intermediate velocities (group 2)) have generally low relative weights. They give some contribution to the Leibowitz & Danziger spectra (Table 3), and even less to Blair et al (Tables 4-6). The weights of the high velocity clouds (group 3)) in the Leibowitz & Danziger and Blair et al. spectra are low relative to those of the low velocity clouds (group 1) particularly for D9, D38,40, D63,64, SWD9, D9,10, and D25.

High velocity models do not contribute to the spectra observed in some of the NE regions (D55, D56, D61, P2D1). Particularly, radiative high velocity shocks are not found in these regions. This indicates that the conditions in the outer region of Kepler SNR are not homogeneous, showing different densities, dust-to-gas ratios, and different grain sizes.

On the other hand, high V_s clouds are present in regions D3, D18, and D27. The line profiles of [NII] 6548, [NII] 6583, and of H α calculated by model MB3 for region D3 (Table 4) are presented in Fig. 2. The line profiles of [NII] and H α (Fig. 2,) show relative fluxes in agreement with Blair et al. (1991, fig. 3). However, the calculated FWHMs are smaller, because the contribution of the high velocity gas which leads to the best agreement of the calculated with the observed line spectra, appears as a socket in the profiles. In fact, the absolute fluxes

Table 3. Comparison of calculated with observed line ratios ($H\beta=1$)

line	1 obs. ¹	ML1 calc.	2 obs.	ML2 calc	3 obs.	ML3 calc.	4 obs.	ML4 calc.	5 obs.	ML5 calc	6 obs.	ML6 calc.
[OII] 3727+3729	(7)	8.5	-	-	11.	10.5	-	-	7.	9.5	-	-
[NeIII] 3869+3968	0.94	0.6	-	-	-	-	-	-	-	-	-	-
[SII] 4069+4076	1.59	1.87	0.97	1.9	1.42	1.87	1.47	1.58	1.33	1.8	-	-
[OIII] 4363	0.2	0.3	-	-	0.27	0.24	0.12	0.27	-	-	-	-
HeII 4686	(0.01)	0.04	-	-	-	-	0.06	0.07	-	-	-	-
[OIII] 5007+	3.32	3.99	3.08	3.2	2.7	2.88	3.4	3.59	3.78	4.2	2.02	2.26
[FeII] 5159	0.25	0.27	(0.03)	0.25	0.17	0.28	0.29	0.3	0.12	0.33	0.05	0.27
[NI] 5199+ 5200	0.03	0.07	(0.07)	0.06	0.11	0.10	0.05	0.1	0.05	0.117	-	-
[FeIII] 5270	0.10	0.29	-	-	0.04	0.3	0.07	0.2	0.05	0.26	-	-
[NII] 5755	0.15	0.49	-	-	0.20	0.5	0.18	0.4	0.09	0.4	0.05	0.5
HeI 5876	0.16	0.18	-	-	0.13	0.17	0.11	0.18	0.06	0.2	0.08	0.156
[OI] 6300+6364	1.5	1.1	1.03	0.94	1.84	1.11	1.83	1.21	1.41	1.46	0.84	0.98
[NII] 6548+6583	6.94	5.4	6.13	5.56	7.69	5.9	7.0	4.82	8.2	5.5	5.97	6.1
[SII] 6717	0.52	0.50	0.36	0.4	0.72	0.75	0.51	0.61	0.66	0.77	0.67	0.64
[SII] 6730	1.02	0.83	0.80	0.75	1.41	1.00	1.04	1.08	1.42	1.13	1.28	1.0
c^2	1.51	-	2.45	-	1.26	-	1.28	-	1.35	-	1.42	-
w(m1)	-	3	-	3	-	10	-	0	-	3	-	15
w(m3)	-	5	-	7	-	9	-	2	-	2	-	12
w(m4)	-	0	-	0	-	0	-	1.5	-	0	-	0
w(m5)	-	3	-	3	-	3	-	0	-	0	-	3
w(m6)	-	3	-	3	-	3	-	1.5	-	3	-	3
w(m7)	-	1	-	1	-	1	-	0	-	0	-	1
w(m8)	-	0	-	0	-	7	-	0	-	0	-	7
w(m9)	-	1	-	1	-	4	-	2	-	1	-	4

¹ observations by Leibowitz & Danziger (1983, Table 3);² adopted for the dereddened spectra.**Table 4.** Comparison of calculated with observed line ratios ($H\beta=1$)

line	D3	MB3	D9	MB9	D18	MB18	D34,35	MB34	D38,40	MB38	
region	SW	-	SW	-	SW	-	SW	-	SW	-	
	obs. ¹	calc.	obs.	calc	obs.	calc.	obs.	calc.	obs.	calc.	
[OIII]4959+5007	2.92	2.91	1.82	1.84	1.186	1.13	-	-	2.17	2.15	
[NII] 5755	0.22	0.5	0.18	0.5	0.188	0.5	-	-	0.148	0.57	
HeI 5876	0.19	0.166	0.116	0.15	0.215	0.17	0.15	:	0.196	0.08	0.15
[OI] 6300+6364	0.79	1.13	1.0	1.08	2.58	2.0	1.39	1.16	0.734	0.64	
[NII] 6548+6583	5.87	5.9	6.09	6.3	9.2	6.4	5.07	5.2	3.76	6.11	
[SII] 6717	0.96	0.83	0.67	0.78	1.28	1.9	0.39	0.47	0.2	0.26	
[SII] 6730	1.59	1.1	1.30	1.1	2.55	2.0	0.78	0.85	0.38	0.59	
$H\alpha^2$	69.	-	164.	-	74.2	-	39.5	-	136.6	-	
E(B-V) ³	0.8969	-	0.8034	-	0.9648	-	0.9005 ⁴	-	0.9077	-	
w(m1)	-	12	-	20	-	10	-	3	-	25	
w(m3)	-	12	-	12	-	10	-	7	-	5	
w(m4)	-	0	-	0	-	0	-	0	-	8	
w(m5)	-	3	-	3	-	0	-	3	-	1	
w(m6)	-	3	-	3	-	1	-	7	-	2	
w(m7)	-	1	-	1	-	0	-	1	-	0	
w(m8)	-	1.8	-	1	-	4	-	0	-	4	
w(m9)	-	6	-	6	-	15	-	1	-	0	
CF (10^{-10})	-	1.5	-	3.	-	0.5	-	5.9	-	2.3	

¹ observations by Blair et al (1991, Table 2)² in 10^{-15} erg cm $^{-2}$ s $^{-1}$ ³ reddening correction assumes intrinsic $H\alpha/H\beta=3.0$ ⁴ a E(B-V)=0.9005 means that extinction of bright filaments is assumed.

Table 5. Comparison of calculated with observed line ratios ($H\beta=1$)

line region	D63,64 SE obs. ²	MB63 - calc.	D55 NE obs.	MB55 ¹ - calc	D56 NE obs.	MB56 - calc.	D61 NE obs.	MB6 - calc	P2D1 NE obs.	MBD1 - calc.	SWD9 SW obs.	MBD9 - SW calc.
[OIII] 4959+5007	-	-	0.17+	0.79	-	-	1.15	1.74	-	-	-	-
[NII] 5755	-	-	-	-	-	-	-	-	-	-	-	-
HeI 5876	-	-	0.037	-	-	-	-	-	-	-	-	-
[OI] 6300+6364	2.97:	2.06	0.36+:	0.5	-	-	0.53 :	0.72	3.64	2.45	1.24	1.1
[NII] 6548+6583	6.19	4.03	1.97	3.9	4.08	3.	5.8	5.8	0.8	2.86	9.88	4.14
[SII] 6717	0.56	0.61	0.092	0.06	0.38	0.37	0.24	0.24	-	-	1.35	0.93
[SII] 6730	1.28	1.25	0.20	0.14	0.91	0.8	0.64	0.53	-	-	2.68	1.7
$H\alpha^3$	12.6	-	33.4	-	22.9	-	18.2	-	20.6	-	34.8	-
E(B-V) ⁴	0.9005	-	0.8926	-	0.9005	-	0.9005	-	0.9005	-	0.9005	-
w(m1)	-	5	-	0	-	0	-	0	-	0	-	4
w(m3)	-	0	-	0	-	0	-	3	-	0	-	0
w(m5)	-	0	-	0	-	1	-	0	-	0	-	0
w(m6)	-	1	-	0	-	0	-	1	-	1	-	0
w(m7)	-	0	-	0	-	0	-	0	-	0	-	0
w(m8)	-	0	-	0	-	0	-	0	-	0	-	1
w(m9)	-	0.01	-	0	-	0	-	0	-	0	-	0

¹ $V_s=55 \text{ km s}^{-1}$ and $n_0=2 \times 10^4 \text{ cm}^{-3}$ ² observations by Blair et al (1991, Table 2)³ $10^{-15} \text{ erg cm}^{-2} \text{ s}^{-1}$ ⁴ see comment about E(B-V) in the bottom of Table 4.**Table 6.** Comparison of calculated with observed line ratios ($H\beta=1$)

line region	D9,10 SW obs. ¹	MB10 - calc.	D25 SW obs.	MB25 - calc	D27 SW obs.	MB27 - calc.	D3 SW obs.	MB3* - calc.	D9 SW obs.	MB9* - calc	D18 obs.	MB18* calc.
[OIII] 4959+5007	0.5+;	0.4	0.65+	0.87	3.18	3.2	2.91	3.0	1.84	1.4	0.51+	1.13
[NII] 5755	-	-	0.12	0.5	0.20	0.4	0.5	0.2	0.5	0.18	0.17	0.5
HeI 5876	-	-	0.12	0.139	0.15	0.15	0.17	0.19	0.15	0.2	0.18	0.17
[OI] 6300+6364	1.71	1.6	1.78	1.32	1.36	1.16	1.13	1.2	1.08	1.3	2.33	2.0
[NII] 6548+6583	7.95	7.88	7.55	7.75	7.18	7.1	5.9	3.2	6.3	3.9	8.77	6.4
[SII] 6717	0.92	1.58	0.815	1.2	0.57	1.0	0.83	0.85	0.78	0.7	1.32	1.9
[SII] 6730	1.97	1.84	1.67	1.6	1.18	1.5	1.1	1.4	1.32	1.1	2.55	2.0
$H\alpha^2$	213.4	-	127.	-	1026.7	-	83.	-	215.8	-	56.	-
E(B-V) ³	0.9005	-	1.0277	-	0.8097	-	0.8804	-	0.8048	-	0.9186	-
w(m1)	-	5	-	7	-	9	-	12	-	20	-	10
w(m3)	-	0	-	0	-	0	-	12	-	12	-	10
w(m5)	-	0	-	0	-	0	-	3	-	3	-	0
w(m6)	-	0	-	0	-	0	-	3	-	3	-	1
w(m7)	-	0	-	0	-	0	-	1	-	1	-	0
w(m8)	-	0	-	1	-	8	-	18	-	1	-	4
w(m9)	-	1	-	1	-	1	-	6	-	6	-	15
CF (10^{-11})	-	7.	-	4.5	-	46.	-	-	-	-	-	-

¹ observations by Blair et al (1991, Table 2)² $10^{-15} \text{ erg cm}^{-2} \text{ s}^{-1}$ ³ see comment about E(B-V) in the bottom of Table 4.

of the $H\beta$ lines ($H\beta_{abs}$ Table 1, last row) and of the [NII] lines ($[NII]/H\beta \times H\beta_{abs}$) are low for high V_s models.

3.3. The SED of the continuum

The data in the X-ray come from Becker et al. (1980), Tuhoy et al. (1979), in the radio from DeLaney et al (2002) and in the IR from Arendt (1989), Saken et al. (1992), and Braun (1997).

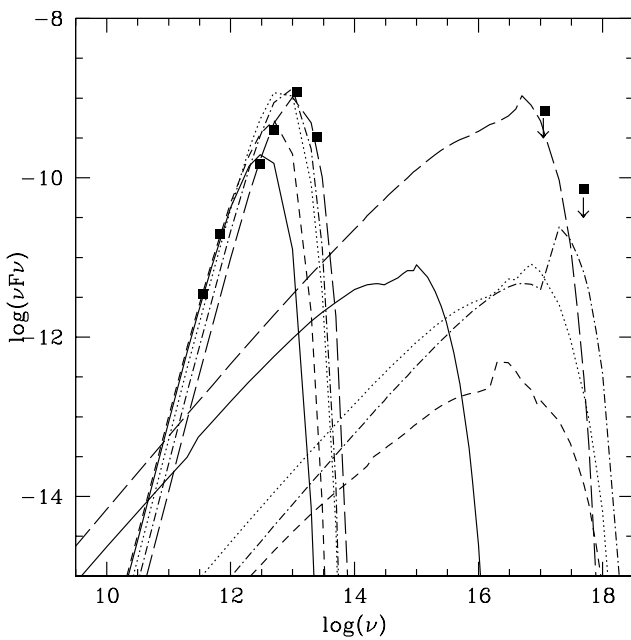


Fig. 3. Comparison of single-cloud models with observational data (black squares). m3 : solid lines; m6 : long-dashed lines; m7 : dotted lines; m9 : short-dashed lines; m10 : dash-dotted lines

Very recently the SCUBA data at 450 and 800 μm by JCM telescope on Mauna Kea were presented by Morgan et al. (2003).

Indeed the data sets in the radio and IR ranges are quite complete and allow the modeling of gas and dust emissions (Figs. 3 and 4). However, data in the optical-UV range are lacking. As a first check, we will constrain the models by the X-ray data, although they are upper limit.

The modeling of the continuum SED must be consistent with that of the line spectra. The SED shows different contributions to the flux in the different frequency ranges. The gas which is heated in the immediate post shock region to relatively high temperatures, cools down downstream with cooling-rates which depend strongly on the gas density, on the relative abundances of the most coolant elements, and on the dust-to-gas ratio. So, the bremsstrahlung emitted from gas in different conditions covers a large range of frequencies, from radio to X-ray. Diffuse radiation from the hot gas maintains the gas ionized and heated to $T \leq 10^4$ K in a relatively large zone downstream.

The optical-UV radiation flux is emitted from gas at $T = 10^4\text{-}10^5$ K, while the soft X-ray domain shows the bremsstrahlung from high temperature gas.

The IR bump corresponds to reradiation by dust. Mutual heating of dust and gas throughout the shock front and downstream leads to dust temperatures which depend on the gas temperatures and, thus, on V_s . Therefore, the frequency corresponding to the peak of dust reradiation is generally determined by V_s (see Contini, Viegas & Prieto 2004). The intensity of the IR flux depends, however, mainly on d/g. The IR bump defined by the observations must be disentangled into the different components corresponding to the different single-cloud models which are used to explain the line spectra.

The modeling procedure starts by fitting the bremsstrahlung which indicates the range of the shock velocity, consistently with the frequency peak in the IR. Then, the IR bump is shifted along the Y-axis by changing the dust-to-gas ratio (Contini et al. 2004), in order to obtain the best fit to the data.

In the radio range, synchrotron radiation generated by Fermi mechanism at the shock front, generally dominates in SNRs. Recall that the character of optical and X-ray magnetobremsstrahlung resembles that of the radio counterpart, but to produce radiation at optical and X-ray frequencies, the electrons must possess considerably higher energies than for radiation in the radio range, or the strength of the magnetic field must be higher (Ginzburg & Syrovatskii 1965). So, the synchrotron radiation is cut at 10^{13} Hz in Fig. 4 as an upper limit.

The SEDs of some significant models are presented in Fig. 3. The fluxes are shifted in order to fit as much as possible the data.

Model m3 is selected as representative of low velocity shocks (group 1), model m6 of intermediate shocks (group 2), model m7 of high velocity shocks (group 3), and model m9 is selected because it is characterized by a high V_s , a low n_0 , and a high d/g. We have added in Fig. 3 the continuum SED of model m10 corresponding to $V_s=1000 \text{ km s}^{-1}$, $n_0=100 \text{ cm}^{-3}$, $d/g=5 \text{ } 10^{-15}$, $a_{gr}=1 \mu\text{m}$, and $D=2 \text{ } 10^{16} \text{ cm}$, which is matter-bound. In fact, the gas downstream contains only the high temperature region, so, the cooling time is smaller than 2 yr. The corresponding radiation-bound model with $D=10^{18} \text{ cm}$ (model m10 in Table 1) would lead to cooling times of ~ 400 yr, i.e. of the same order of the remnant age, because d/g is low. Model m10 shows that non radiative shocks can contribute strongly to the soft X-rays and to IR radiation. However, in region dominated by grains small enough to be destroyed by sputtering, this type of models contributes only to the bremsstrahlung.

The fluxes of models m7 and m9 displayed in Fig. 3 are multiplied by a factor of $4 \cdot 10^{-11}$ in order to fit the data. Those of models m3 and m6 are multiplied by factors of $8.1 \cdot 10^{-9}$ and $4 \cdot 10^{-9}$, respectively, and the flux of model m10 by a factor of $1.6 \cdot 10^{-10}$. Recall that models are calculated at the nebula while the data are observed at Earth. Therefore, conversion factors which account for the distances of the observed regions from the remnant center and of the remnant to Earth must be considered. The modeling of the line spectra shows (Sect. 3.2) that the observed regions are explained by multi-cloud models, so, in this first analysis of single-cloud models, only the ratios of these factors are significant because they show the ratio of the flux intensities from different models.

Fig. 3 shows that the IR flux calculated by model m3 peaks at lower frequency than model m6 because V_s is lower. The high post shock temperature region corresponding to model m9 with $V_s=1000 \text{ km s}^{-1}$, is reduced by the strong cooling due to the high d/g, so, the peak in the IR, as well as the bremsstrahlung peak, appear shifted to lower frequencies. The bremsstrahlung of model m3 corresponding to low V_s is not constrained by the soft X-ray upper limits, therefore, the dust-to-gas ratio cannot be confirmed. Recall that in both m3 and m6 $d/g = 10^{-14}$ by number (corresponding to $4 \cdot 10^{-4}$ by mass for silicates) is adopted. Fig. 3 shows that the calculated IR bumps

of the models fit most of the IR data well enough to confirm that these types of clouds contribute to the SED of Kepler's SNR.

However, the observational data correspond to the whole SNR. So, as a second step in modeling the continuum SED, we compare the data with a model which accounts for the most luminous regions observed by Blair et al, (D3, D9, D18, D34,35, D38,40, D9,10, D25, D27). Therefore, first, the continuum corresponding to the multi-cloud model which explains the line spectrum is calculated for each observed region. Then, the results are summed up adopting conversion factors (CF) which are the same for the continuum and line spectra from each region. The CF are, therefore, calculated from the observed $H\alpha$ fluxes given by Blair et al in the different regions, and included in Tables 4-6, and from the calculated $H\beta$ fluxes, which are given in Table 1 for the different models. $H\alpha/H\beta=3$ is adopted. The calculated CF for each region appear in the bottom of Tables 4-6. Multiplying these CF by the continua emitted from each region and summing up, the total continuum SED is approximatively calculated for the Kepler SNR and can be compared with the data.

In Fig. 4 the bremsstrahlung is indicated by a solid line, while dust emission by a dashed line. We have separated the dust emission curve from the bremsstrahlung to better understand their roles. Model m10, represented by dotted lines, has not been included in the sum.

ISOCAM observations presented by Douvion et al (2001) in different regions, cover the range between $6.5 \mu\text{m}$ and $16 \mu\text{m}$. We have summed up the fluxes from the different regions corresponding to $12 \mu\text{m}$ and $16 \mu\text{m}$ and they are shown in Fig. 4 for comparison.

To further check whether the calculated total bremsstrahlung in the optical range is consistent with the observations, the continuum flux at 5400 \AA is roughly deduced from the spectrum observed by Leibowitz & Danziger (1983, Fig. 3) and is indicated as an open square in Fig. 4. The constraint of the continuum SED is acceptable and confirms that the dust-to-gas ratios adopted in single-cloud models, are reliable. Nevertheless, Fig. 4 shows that the two IR data at 60 and $100 \mu\text{m}$ are overpredicted by the models. A better fit could be obtained considering the observation error and/or by reducing the weight of models m7-m8 and/or by reducing the d/g ratio of these models. A lower d/g leads to large cooling times downstream of models m7 and m8, so that the model parameters should be rearranged destroying the good fit the line spectra. A lower weight, too, leads to changes in some multi-cloud line spectra. Indeed, the fits of the observed continuum and of the line spectra could be improved separately. However, model results for continuum and line spectra are cross-checked, leading to the best modeling of both.

The synchrotron radiation calculated in the radio range is represented by a thin solid line in Fig. 4. DeLaney et al. (2002) find a mean value in the spectral index of -0.71 for synchrotron radiation in the radio range, which generally originates from turbulence and magnetic field enhancement at the shock fronts in SNR. The present modeling shown in Fig. 4, adopting Fermi mechanism at the shock front (Bell 1978) leads to a spectral index of 0.75 , which explains satisfactorily the data. Moreover,

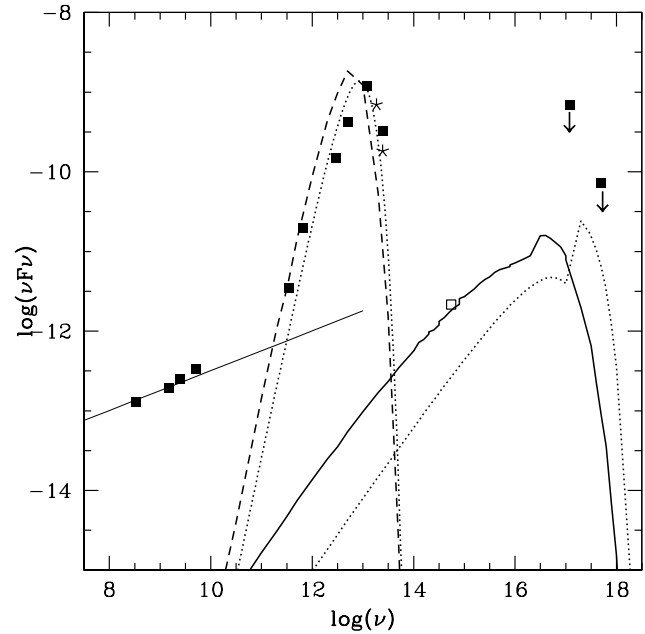


Fig. 4. Consistent modeling of the Kepler SNR continuum SED by the summed model (thick solid line : bremsstrahlung; thin solid line : synchrotron radiation; dashed line : IR emission) and model m10 (dotted lines). The observational data are represented by black squares. The datum at 5400 \AA from Leibowitz & Danziger (1983) is represented by an open square. The asterisks refer to Douvion et al (2001a)

the difference in structure between the flat and steep spectra of radio emission is explained by DeLaney et al. by a partial decoupling of the forward and reverse shock. Although we find that both types of shocks act in nearly all the observed regions, it is difficult to predict how much they have farthened at the time of observations.

Summarizing, it is found by modeling that dust-to-gas ratios are $4 \cdot 10^{-4}$ by mass in clouds corresponding to low velocity shocks and even lower in intermediate velocity clouds. On the other hand, d/g are relatively high in clouds corresponding to high velocity shocks, by factors of 4 , 6 , and 9 for V_s of 700 , 800 , and 1000 km s^{-1} , respectively.

4. Discussion and concluding remarks

In this work the calculation of dust emission is carried out consistently with emission from gas for both line and continuum spectra, leading to the evaluation of the dust-to-gas ratios in the Kepler SNR. A successful application of this method (Contini et al 2004) was presented for luminous IR galaxies (Contini & Contini 2003) and for AGN (e.g. Contini & Viegas 2000).

The two component emission observed in the FWHM of the $H\alpha$ line profiles corresponding to velocities of $\sim 50 \text{ km s}^{-1}$ and $\sim 1000 \text{ km s}^{-1}$ is confirmed by modeling. They correspond to the reverse and the expanding shocks, respectively, and are explained by the supernova interaction with a stellar wind.

A grid of single-cloud models is calculated. The models cover the set of physical conditions in the emitting gas that are

revealed by the line ratios and by the FWHM of the line profiles. Multi-cloud models which account for the reverse and expanding shock in each region, are adopted in order to fit the line spectra in the different observed regions and the corresponding continuum SED. The total continuum which results from summing up the contributions of the most luminous regions, is compared with the observed continuum SED. Dust emission in the IR is consistently calculated. The ratio between dust emission and bremsstrahlung in the IR range depends on the dust-to-gas ratios adopted in the models.

The high dust-to-gas ratios which are found by modeling the IR bump in models corresponding to high velocity shocks, speed up the cooling rate downstream, leading to radiative shocks even in a relatively low density gas. It is found that radiative high velocity shocks are absent in the NE region of the remnant, suggesting that d/g is low and/or the grains are small enough to be destroyed by sputtering. This result may indicate that dust is not homogeneously distributed throughout the remnant.

Moreover, Kepler SNR morphological structure in the different wavelengths can be explained by model results. In fact, the X-ray emission has the same shell-like morphology and is qualitatively similar to the radio emission (Blair et al, DeLaney et al.), confirming that both radio and X-ray are created at the shock front of the expanding shock. Indeed, the high temperatures ($> 10^7$ K) of the gas in the immediate post-shock region downstream, correspond to the X-ray emission.

The $H\alpha$ and IR images are also similar (Blair et al.) and are similar to the X-ray image as well. Particularly, the striking similarity between the $H\alpha$ and IR images suggests that the 12 μm thermal dust emission and the optical emission have the same origin (DeLaney et al. 2002) confirming that dust grains are collisionally heated by the gas across the shock fronts and downstream. The regions of dissimilarity could be explained by the inhomogeneous distribution of dust grains.

Notice that the modeling of the Kepler SNR through the line and continuum spectrum analysis in the different regions is presented in previous sections with the aim of calculating the dust-to-gas ratios. Actually, this work has been inspired by Morgan et al (2003) who claim that dust formation in supernovae is required to be an important process relative to the age of the Universe.

Morgan et al calculate that the maximum dust mass swept up by the SNR is $\sim 10^{-3} M_\odot$, assuming a maximum density $n = 0.1 \text{ cm}^{-3}$ and a gas to dust ratio of 160. However, adopting a higher n (100 cm^{-3}) the dust mass swept up is $\sim 1 M_\odot$. Douvion et al (2001) claim that by using dust grains of 'astronomical silicates' both mid-IR ISOCAM and IRAS data can be fitted by a single grain temperature of 107 K, while previous models required two dust components : a hot dust of 140 K and a cold one of 54 K (Saken et al. 1992). The total mass calculated by them is $10^{-4} M_\odot$.

The model presented in this work shows that two main types of dust lead to a good fit of the IR bump consistently with the bremsstrahlung. Large grains with $a_{gr}=1 \mu\text{m}$ with $d/g < 4 \cdot 10^{-3}$ survive sputtering downstream of the expanding shock and are collisionally heated to a maximum temperature of 125 K. Smaller grains ($a_{gr}=0.2 \mu\text{m}$) downstream of the re-

verse shock (Fig. 1) with dust-to-gas ratios of $\sim 4 \cdot 10^{-4}$ are heated to a maximum temperature of ~ 50 K.

Adopting a SNR diameter of 3.8 pc, a pre-shock density $\sim 50 \text{ cm}^{-3}$ by the average of models m7, m8, m9 (Table 1) (Sect. 3.3), we obtain a swept up gas mass of $40 ff M_\odot$ and a maximum dust mass of $0.16 ff M_\odot$, where $ff \leq 1$ is the filling factor.

Such relatively high pre-shock densities in single clouds are justified by the relatively young age of Kepler SNR. In older SNR (e.g. the Cygnus Loop), n_0 is less than 10 cm^{-3} (Contini et al 1980). Moreover, the clumpy aspect of the remnant suggests that average densities on large scales are not realistic and that ff should be ≤ 0.1 .

Comparing with other SNR, Douvion et al (2001a) found that a dust mass of $10^{-4} M_\odot$ results from the warm component (140 K as for Kepler SNR) and of $4 \cdot 10^{-3} M_\odot$ for the cold component (55 K) of Tycho. They claim that the Crab nebula IR emission is dominated by synchrotron radiation and no dust is detected. In Cassiopeia A the dust is made of more components, e.g. quartz and aluminum oxid, besides silicates which have a mass of $7.8 \cdot 10^{-9} M_\odot$ (Douvion et al 2001b).

Acknowledgments

I am very grateful to an anonymous referee whose precious comments helped to improve the paper and to Elia Leibowitz for fruitful discussions.

References

- Allen, C.W. 1973, *Astrophysical Quantities* (London: Athlon)
- Arendt, R.G. 1989, *ApJS*, 70, 189
- Baade, W. 1943 *ApJ*, 97, 119
- Bandiera, R., 1987, *ApJ*, 319, 885
- Bell, A.R. 1978, *MNRAS*, 182, 443
- Becker, R.H., Boldt, E.A., Holt, S.S., Serlemitsos, P.J., White, N.E., 1980, *ApJ*, 237, L77
- Blair, W.P., Long, K.S., Vancura, O. 1991, *ApJ*, 366, 484
- Broun, R. 1987, *A&A*, 171, 233
- Chevalier, R. & Oishi, J. 2003, *astro-ph/0306376*
- Contini, M. 1987, *A&A*, 183, 53
- Contini, M. & Contini, T. 2003, *MNRAS*, 342, 299
- Contini, M. & Shaviv, G. 1982, *ApSS*, 85, 203
- Contini, M., Shaviv, G., & Kozlovsky, B.Z., 1980, *A&A*, 92, 203
- Contini, M. & Viegas-Aldrovandi, S.M. 1990, *ApJ*, 350, 125
- Contini, M. & Viegas, S.M. 2000, 535, 721
- Contini, M. & Viegas, S.M. 2001, *ApJS*, 132, 211
- Contini, M., Viegas, S.M., & Prieto, M.A. 2004 *MNRAS*, 348, 1065
- Cox, D.P. 1972, *ApJ*, 178, 143
- Decourchelle, A. & Petre, R. 1999, *AN*, 320, 203
- DeLaney, T., Koralesky, B., & Rudnick, L. 2002, *ApJ*, 580, 914
- Dennefeld, M. 1982 *A&A*, 112, 215
- D'Odorico, S., Bandiera, R., Danziger, J., Focardi, P. 1986, *AJ*, 91, 1382
- Douvion, T., Lagage, P.O., Cesarsky, C.J., Dwek, E. 2001a *A&A*, 373, 281
- Douvion, T., Lagage, P.O., Pantin, E. 2001b *A&A*, 369, 598
- Draine, B.T. 1981, *QpJ*, 245, 880
- Dwek, E. & Arendt, G. 1992, *ARAA*, 30, 11
- Dwek, E., Foster, S.M., & Vankura, O. 1996, *ApJ*, 457, 244
- Ginsburg, V.L. & Syrovatskii, S.I. 1965, *ARA&A*, 3, 297

Hughes, P. 1999 ApJ, 527, 298

Leibowitz, E.M. & Danziger, I.J. 1983 MNRAS, 204, 273

Morgan, H.L., Dunne, L., Eales, S.A., Ivison, R.J., Edmunds, M.G. 2003, *astr-ph/0309233*

Saken, J.M., Fesen, R.A., Shull, J.M. 1992, ApJS, 81, 715

Sollerman, I., Ghavamian, P., Lundqvist, P., Smith, R.C. 2003, A&A, 407, 257

Tuohy, I.R., Nugent, J.J., Garmire, G.P., Clark, D.H., 1979, Nature, 279, 139

van den Bergh, S. & Kamper, K.W. 1977, ApJ, 218, 617

Viegas, S. M. & Contini, M., 1994, ApJ, 428, 113